Available online at www.sciencedirect.com

ScienceDirect

IFAC Papers Online CONFERENCE PAPER ARCHIVE

IFAC PapersOnLine 51-15 (2018) 981–989

Modeling, Identification, Estimation and Adaptation for the Control of Power-Generating Kites [1]

Tony A. Wood * **Henrik Hesse** ** **Max Polzin** * **Eva Ahbe** *
Roy S. Smith *,[2]

* *Automatic Control Laboratory, Swiss Federal Institute of Technology (ETH), Zürich, Switzerland.*
** *University of Glasgow, Singapore.*

Abstract: Large-scale kites, flying high-force crosswind trajectories, have been proposed for wind power generation. A two phase operational cycle generates net positive power using a ground-based motor/generator. In the traction phase the kite flies a high-force trajectory while reeling out the generator-connected tethers. A low-force retraction phase reels in the tethers and returns the kite to the start of the cycle. Highly variable conditions and significant uncertainty in the dynamics pose challenges to autonomous, well-controlled flight. The control task is divided into trajectory generation and tracking components and the most uncertain parameters in the model are identified online. The control structure uses these parameters in a robust framework resulting in an experimentally verified adaptive control scheme.

Keywords: Airborne wind energy, Kite dynamics, Identification, Adaptive control, Estimation.

1. INTRODUCTION

Airborne Wind Energy (AWE) uses tethered flying vehicles to generate electrical power. The concept was first proposed by Loyd 1980 using a kite flown in a cross-wind pattern. The idea only began to be exploited more widely after 2000. Early work in the area was carried out by Diehl (2001); Houska and Diehl (2006), Ockels (2001), Lansdorp and Ockels (2005), Canale et al. (2007); Fagiano (2009) and Breuer and Luchsinger (2010). More recently many other researchers and start-up companies started contributing to the field. A related application is the use of kites for towing sea-going vessels (Erhard and Strauch (2013)). Several start-up companies have flown developmental prototypes but none have yet begun commercial-scale production.

Almost all AWE systems exploit the force generated in cross-wind flight in one of two ways. Airborne generation systems mount propellor-driven generators on the flying vehicle, with the most developed system being that by Makani (2018). These systems require a rigid wing for generator mounting and a conductive cable for transmitting the power to the ground.

A more common alternative is the use of tethered wings and ground-based generation via winched tethers. This configuration may use a soft kite or rigid wing and can be actuated directly from the ground. These systems are typically lower cost and lower risk which has made them popular with research groups and start-up companies. Schmehl (2018) gives descriptions of many such systems. Actuating the vehicle from the ground introduces additional control and estimation challenges which we discuss in this paper.

The modeling and control methods developed in Fagiano et al. (2014) and Zgraggen et al. (2015) form the basis for the work we present here. Rigid kites offer more flexibility in terms of on-board actuation and this can alleviate some of the uncertainty in the dynamics, as well as reducing the significant delay that comes from ground-based actuation. Our work on rigid kite control is summarised in Luchsinger et al. (2018). In this paper we focus on soft kites and in particular the modeling and online identification required to implement an adaptive control scheme capable of handling the significant uncertainties in the dynamics.

Section 2 describes the AWE system and a simple model of the kite dynamics. The control architecture is given in Section 3 and Section 4 describes the online identification of key model parameters required for control. The sensing options and estimation structure are described in Section 5 and experimental verification of adaptive kite control is presented in Section 6.

2. AIRBORNE WIND ENERGY SYSTEMS

2.1 Ground-based generation

The basic two-phase operational concept is illustrated in Figure 1. The kite has a lift force generating cross-section and this is the basis for power generation. During a reel-out phase the kite is repeatedly flown in a high force cross-wind figure-of-eight pattern and generates power by unreeling

[1] This work supported by the Swiss National Science Foundation (141836), the Swiss Commission for Technology & Innovation (15844.1 & 18212.1), the Swiss Secretariat for Education, Research & Innovation (15.0065), and the EU Marie Curie-Skłodowska (642682).
[2] Corresponding author. (rsmith@control.ee.ethz.ch)

10.1016/j.ifacol.2018.09.066

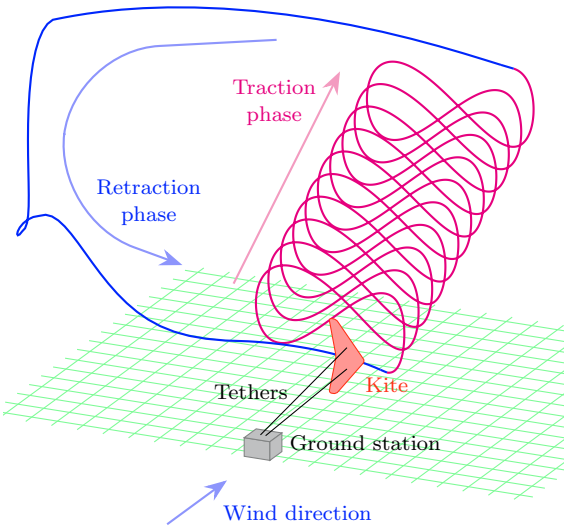

Fig. 1. Ground-based generation concept. Power is generated in the traction phase, and the kite is recovered during the retraction phase.

tethers connected to a generator. When the maximum reel-out of the tethers is reached a lower force trajectory is flown to allow the kite to be retracted with a significantly lower energy expenditure. A prototype system with a wing area of 6 m^2 has been able to generate an average power of approximately of approximately 330 W. (Zgraggen (2015)) over such a two-phase cycle. A start-up design (TwingTec (2018)) uses an optimised rigid-wing design to give an average power of 100 kW. with a wing span of 15 m.

The reel-out speed of the kite is slow compared to its velocity and so the kite can be considered as being constrained to fly on the surface of a sphere. The quarter-sphere downwind of the ground station is referred to as the wind window. Maximum power is extracted when the kite flies perpendicular to the wind and the power drops off as the kite heads towards the edges of the wind window. As the kite moves upward on the sphere the power drops as a result of the decreasing angle with respect to the wind velocity. However, increasing altitude typically leads to increasing wind velocity and greater power extraction. The optimal trade-off between these effects will depend on local wind conditions.

We will consider a two-line tethered kite with independent control of the length of each tether. The difference in tether length rolls the kite and provides a turning actuation. This is decoupled from the common reel-out of the tethers which is used to transfer force from the kite tethers to torque on the ground-based winch/generator. The tethers are connected to the kite via bridle lines, illustrated schematically in Figure 2. The bridle lines transmit the force from the kite to the tethers and their configuration determines the kite's angle-of-attack and the lift (and drag) force relationship with respect to the apparent wind. In practice bridle lines may also connect at other points, particularly the leading and trailing edges of the kite. The kite may also have stiffening elements in order to create a lift-generating cross-section.

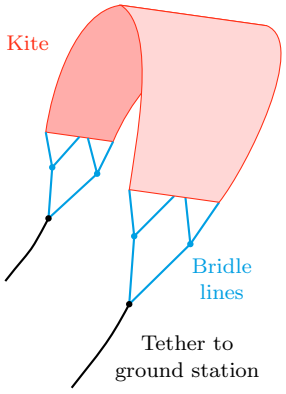

Fig. 2. Illustrative tether and bridle arrangement for a soft kite configuration.

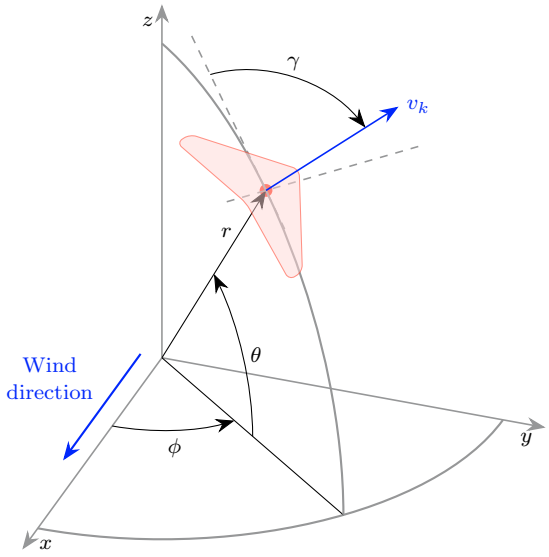

Fig. 3. Kite coordinate system. The kite's tangential velocity is v_k and the angle between v_k and the zenith on the tangential plane is the heading angle, γ. The x-axis is aligned with the wind direction.

2.2 Kinematic model

The position of the kite will be defined in terms of the elevation angle, θ, the azimuth angle, ϕ, and the distance of the kite from the ground station, r. These definitions are illustrated in Figure 3. For simplicity we are considering the case where the wind is parallel to the x axis.

We will assume that the reel-out velocity, $\dot{r}$, is small compared to the kite's forward velocity, v_k, and so the kite is modeled as being constrained to the surface of a sphere of radius r. The velocity vector, v_k, is tangent to the sphere. The heading angle, γ is defined as the angle between v_k and the zenith, projected onto the tangent plane of the sphere,

$$\gamma = \arctan\left(\frac{\cos(\theta)\,\dot{\phi}}{\dot{\theta}}\right).$$

Because of the low kite mass, and relatively high aerodynamic forces, it is common to assume that the forces on the kite balance and the kite motion is modeled as a time-varying dynamic equilibrium. For simplicity we

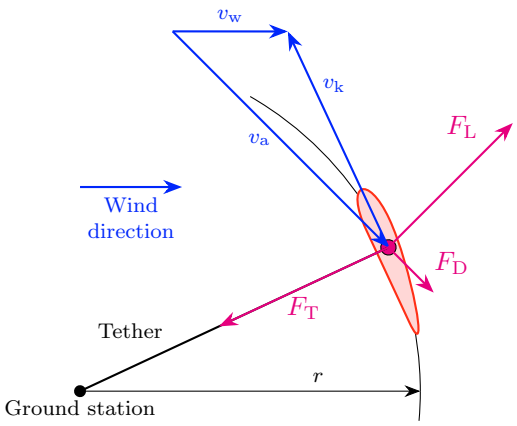

Fig. 4. Kite forces and velocities in the plane defined by r and v_k.

also assume that the reel-out speed of the tether, $\dot{r}(t)$, is negligible compared to the kite speed, v_k. Figure 4 illustrates the result of these assumptions on the kite forces and velocities.

The "apparent wind", v_a, is the wind vector expressed with respect to the kite,

$$v_a = v_w - v_k,$$

and determines the aerodynamic forces that the kite experiences. The lift and drag forces, F_L and F_D respectively, have magnitudes given by,

$$\|F_L\| = \frac{\rho C_L S}{2}\|v_a\|^2 \quad \text{and} \quad \|F_D\| = \frac{\rho C_D S}{2}\|v_a\|^2,$$

where ρ is the atmospheric density, C_L and C_D, are the lift and drag coefficients and S is the wing area. The drag force, F_D, is parallel (and in opposite direction) to v_a, and the lift force, F_L, is perpendicular to F_D in the plane defined by r and v_k. If gravitational and inertial forces are neglected, F_L and F_D are balanced by the force on the tether, F_T, and this enables us to express the apparent wind's tangential component as a function of the kite's position in the wind window, and having magnitude,

$$\|v_{a_{\text{tangential}}}\| \;=\; \|v_w\|\frac{C_L}{C_D}\cos\theta\,\cos\phi.$$

As the kite typically flies at 5 to 10 times the wind speed this is also a rough approximation for the magnitude of the kite velocity,

$$\|v_k\| \;\approx\; \|v_w\|\frac{C_L}{C_D}\cos\theta\,\cos\phi. \tag{1}$$

More accurate models can be derived and Schmehl et al. (2013) provides a good summary. However (1) already shows the dominant sources of variability. The first is the wind speed, v_w, which varies due to gusts and a largely unknown height dependency. The second source of variation enters via the lift and drag coefficients, C_L and C_D. Approximating the aerodynamic forces with these two parameters is a significant simplification, especially in the case of soft kites where shape deformations have a larger effect than in rigid aerofoils.

In the simplest kite configurations the kite is actuated by changing the difference between the two tether lengths. This actuation variable is denoted by u and has the effect of rolling the kite and thereby introducing a change in the heading angle γ. In a flexible kite this is a difficult effect to model. The dominant aspects are a "steering gain", K_s, and a delay, τ_s. This, together with the basic kinematic relationships, leads to a simple unicycle model for the kite.

$$\dot{\theta} \;=\; \frac{v_k}{r}\cos\gamma \tag{2}$$

$$\dot{\phi} \;=\; \frac{v_k}{r\,\cos\theta}\sin\gamma \tag{3}$$

$$\dot{\gamma} \;=\; K_s\,u(t-\tau_s). \tag{4}$$

Similar kite steering models also appear in Erhard and Strauch (2013). Section 4 provides an experimental verification of this form of model.

The steering delay, τ_s, comes from two sources. The first is the delay in actuating the kite via tether length changes. The tethers have non-negligible mass and drag force. These effects are complex and depend on tether length as well as kite velocity. Several authors have developed detailed models of these effects, but the dominant effect on the control is a delay that depends on tether length and kite velocity. The second source of delay arises from the kite position estimation procedure. The simplest kite configuration estimates kite position from tether angle and tether length measurements at the ground station. The tether dynamics also influence these measurements giving an analogous delay to the tether actuation case. Under typical operating conditions for a soft kite the total delay ranges between 0.5 and 1.0 seconds (Polzin et al. (2017)). Section 5 introduces additional sensing modalities which can remove the majority of the delay due to ground-station sensing. Reducing the actuation delay is only possible by augmenting the kite with on-board actuators, and this is generally only possible on rigid kites.

The variation in the steering model gain, K_s, comes from a variety of sources including simplifying the kite velocity dependent effects. The tether bridle holds the kite at a nominally fixed angle-of-attack. In practice this varies causing lift and drag force variations which also influence the turning rate. Soft kites are inherently flexible and as the kite turns it may not maintain the same shape—and therefore the same lift and drag characteristics—as in straight flight. We attempt to capture all of these effects via uncertainty in the K_s parameter.

3. CONTROL SYSTEM ARCHITECTURE

A cascaded control architecture, illustrated in Figure 5, separates the system into trajectory generation and heading angle tracking components. Partitioning the control problem in this manner is also done in Erhard and Strauch (2013), Jehle and Schmehl (2014), and Fagiano et al. (2014). Uncertainty and variation in the steering parameters, K_s and τ_s, limit performance in both the heading angle tracking and guidance controller subsystems. In the traction phase the steering parameters are estimated twice per figure-of-eight cycle and used to ensure robust heading angle tracking performance as well as feasible γ_{ref} guidance control. The choice of two estimates per cycle is a trade-off between having sufficient data for an accurate estimate and tracking a time-varying parameter. The control system has been described in more detail in Wood et al. (2017b).

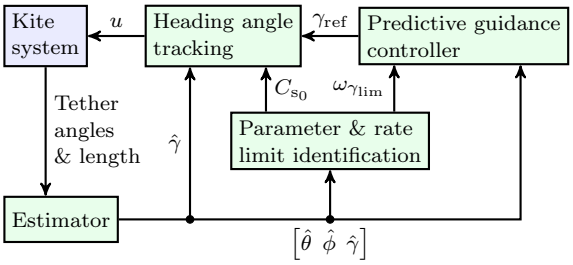

Fig. 5. Kite control architecture. An inner loop controls γ and a cascaded outer loop generates γ_{ref}. Identified parameters are used to adapt the tracking and predictive guidance controllers.

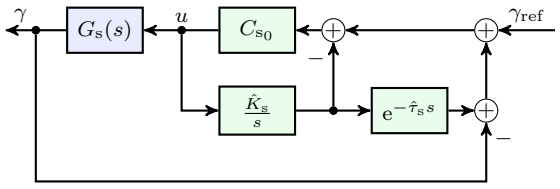

Fig. 6. Smith predictor structure for heading angle tracking. In practice the measurement of γ is replaced by an estimate, $\hat{\gamma}$.

The control components are chosen and designed so that they can be parametrised in terms of K_{s} and τ_{s}. In this way we can maintain robustness with respect to parameter variation and effectively tune the control gains as a function of the operating conditions.

3.1 Heading angle tracking

The inner cascade loop tracks a specified heading angle reference γ_{ref}, using a Smith predictor structure. The advantage of this structure, illustrated in Figure 6, is that it can explicitly account for a delay in those cases where the delay limits the achievable performance. This explicit formulation makes it easy to modify the heading angle tracking controller as a function of the estimated delay.

The kite steering model in (4) is

$$\gamma \;=\; G_{\text{s}}(s)u \;=\; \frac{K_{\text{s}}}{s}\text{e}^{-\tau_{\text{s}}s}u.$$

Although both K_{s} and τ_{s} will be estimated in operation we expect that there will still be some error in these values due to the variations over the course of the traction cycle and variations in the kite dynamics. The estimates and associated bounds are,

$$\hat{K}_{\text{s}} - \delta_{K_{\text{s}}} < K_{\text{s}} < \hat{K}_{\text{s}} + \delta_{K_{\text{s}}} \tag{5}$$

and

$$\hat{\tau}_{\text{s}} - \delta_{\tau_{\text{s}}} < \tau_{\text{s}} < \hat{\tau}_{\text{s}} + \delta_{\tau_{\text{s}}}. \tag{6}$$

As the undelayed part of the steering model, K_{s}/s, is an integrator, choosing C_{s_0} as a static gain provides an ideal loopshape with a crossover frequency of $\omega_{\text{c}} = K_{\text{s}}C_{\text{s}_0}$ rad/sec. The Smith predictor structure effectively delays the feedback comparison with the reference, γ_{ref}, to prevent the delay, $\text{e}^{-\tau_{\text{s}}s}$, from destabilising the loop. Of course this also delays the closed-loop tracking response by $\hat{\tau}_{\text{s}}$ seconds.

Incorporating the control gain C_{s_0} into the Smith predictor structure shown in Figure 6 (and using estimates for the gain and delay) gives the controller,

$$C_{\text{s}}(s) \;=\; \frac{C_{\text{s}_0}}{1 + \frac{C_{\text{s}_0}\hat{K}_{\text{s}}}{s}(1 - \text{e}^{-\hat{\tau}_{\text{s}}s})}.$$

It can be shown (see Wood et al. (2015a)) that if C_{s_0} satisfies

$$C_{\text{s}_0} < \frac{\pi}{2\hat{K}_{\text{s}}\delta_{\tau_{\text{s}}}\sqrt{\left(1 + \frac{\delta_{K_{\text{s}}}}{\hat{K}_{\text{s}}}\right)^2 + 1}}, \tag{7}$$

then the closed-loop reference tracking system is stable for gains and delays that satisfy (5) and (6).

The limit on C_{s_0} in (7) puts an upper bound on the bandwidth of the heading angle tracking controller. This limit, denoted by $\omega_{\gamma_{\text{lim}}}$, is used within the guidance controller (see Section 3.2) to limit the derivative of the heading angle reference to ensure that that commanded heading angle, γ_{ref}, can be tracked. The limit,

$$|\dot{\gamma}_{\text{ref}}| \;<\; \omega_{\gamma_{\text{lim}}}, \tag{8}$$

is also used in the offline calculation of the nominal optimal trajectories described in Section 3.3.

3.2 Trajectory path guidance

The predictive guidance subsystem provides γ_{ref} to the γ tracking controller, $C_{\text{s}}(s)$. This must be done so that the γ_{ref} trajectory can be followed by $C_{\text{s}}(s)$, even as the bandwidth of $C_{\text{s}}(s)$ varies as a function of the online estimates of K_{s} and τ_{s}. Our initial work Wood et al. (2015a)) achieved this via a precalculated series of γ_{ref} trajectories, parametrised by the current $C_{\text{s}}(s)$ bandwidth limitation. Our current approach (see Wood et al. (2017a)) uses a Model Predictive Controller (MPC) to generate γ_{ref}. The problem is formulated as minimising a linear quadratic (LQ) cost based on the difference between the predicted trajectory, γ_{ref}, and an optimal trajectory, γ_{opt}. Section 3.3 outlines a method for the offline calculation of a family of optimal trajectories.

An important feature of the MPC formulation is that the prediction horizon is partitioned into two intervals. The first propagates the predicted kite position based on prior control actions as the actuation delay means that current control actions will have no effect on the kite over this portion of the horizon. The remainder of the horizon can be controlled and the kite is driven towards a power optimal figure-of-eight trajectory subject to constraints.

The problem formulation uses linearised dynamics (derived from (2) and (3)). The frequency band-limit on γ_{ref} was implemented as a limit, (denoted $\omega_{\gamma_{\text{lim}}}$) on the derivative of the heading angle reference, $\dot{\gamma}_{\text{ref}}$. The magnitude of γ_{ref} is also constrained to prevent the kite from being commanded to fly straight down. In the traction cycles the kite traverses edges of the figure-of-eight paths in an upward direction. As an additional safety feature a minimum altitude constraint is also enforced.

3.3 Optimal trajectories

An optimisation approach is used to calculate trajectories, γ_{opt}, for the traction phase. We are looking for a limit

cycle solution to the dynamics, (2)–(4), that maximises the tether force integrated over a single figure-of-eight trajectory with a period T_p. The problem is formulated as follows,

$$\begin{aligned} &\max_{x(\cdot),u(\cdot),x_0,T_\mathrm{p}} && \frac{1}{T_\mathrm{p}}\int_0^{T_\mathrm{p}} F(x(t),u(t))dt \\ &\text{subject to:} && \\ &\forall t\in[0,T_\mathrm{p}]: && \dot{x} = f(x(t),u(t)) \\ & && \underline{c} \le x(t) \le \overline{c} \\ & && \underline{b} \le u(t) \le \overline{b} \\ & && x(0) = x(T_\mathrm{p}) = x_0. \end{aligned}$$

The dynamics of the state, $x(t) = [\theta(t)\ \phi(t)\ \gamma(t)]$ are given by $f(x(t),u(t))$ and also include the kite velocity approximation in (1). The minimum altitude, heading angle, and heading angle rate limits ($|\dot{\gamma}_\mathrm{ref}| < \omega_{\gamma_\mathrm{lim}}$) are imposed as state constraints. The optimal heading angle trajectory, γ_opt, is calculated from the optimal $u(t)$ and $x(t)$.

The cost function, $F(x(t),u(t))$, is an estimate of the tether force exerted by the kite, neglecting any tether reel-out,

$$F(x,u) = \frac{\rho S C_\mathrm{D}}{2}\left(1+\left(\frac{C_\mathrm{L}}{C_\mathrm{D}}-\beta u^2\right)^2\right)^{3/2}(\cos\theta\,\cos\phi\,v_\mathrm{w})^2.$$

The βu^2 term models the loss of lift due to turning manoeuvres. A similar penalisation is used in Costello et al. (2015). Numerical solutions to a discretised version of this problem are calculated offline with the GPOPS-II MATLAB software (Patterson and Rao (2014)).

4. DELAY AND GAIN IDENTIFICATION

The steering model in (4) is obtained empirically, and discussed along with the data presented here in more detail in Wood et al. (2015b). Figure 7 illustrates the correlation between the steering input, $u(t)$, and the rate of change of heading angle, $\dot{\gamma}$. The data is sampled with a period of $T_\mathrm{s} = 0.01$ sec. and has a duration of 80 seconds, representing approximately 13 figure-of-eight manoeuvres. The heading angle derivative is approximated from the data by $\dot{\gamma} \approx (\gamma(t_{k+1}) - \gamma(t_k))/T_\mathrm{s}$. The value of $\gamma(t)$ used here comes from frame transformations of the output of an inertial measurement unit (IMU) flown onboard the kite. As the IMU includes a Kalman filter, the "measurement" of $\gamma(t)$ is actually a filtered estimate and so the $\dot{\gamma}$ approximation does not exhibit significant noise amplification.

The delayed input, $u(t-\tau_\mathrm{s})$, is plotted in Figure 7 for two different delays ($\tau_\mathrm{s} = 0$ and $\tau_\mathrm{s} = 0.66$ sec.). The heading angle derivative has a repeatable relationship with respect to the undelayed input, $u(t)$ but it is far from linear. The delay of $\tau_\mathrm{s} = 0.66$ sec. gives a close to linear estimate, $\hat{K}_\mathrm{s}$, for the steering gain. Figure 7 also highlights the region where $|\phi| < 0.17$ rad. as this represents the region of the wind window which dominates the power production. In this region the fit is very close.

The best estimates for $\hat{K}_\mathrm{s}$ and $\hat{\tau}_\mathrm{s}$ are defined by minimising the RMS error of the model fit,

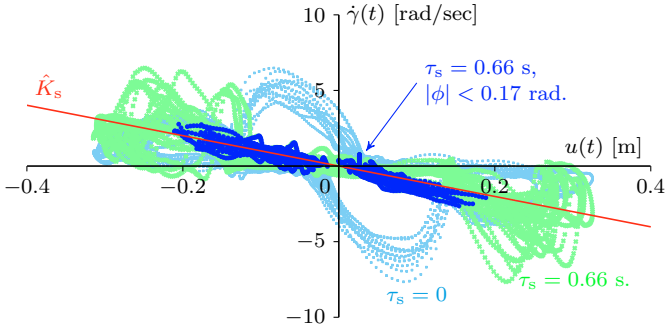

Fig. 7. Steering gain model estimation. A smoothed estimate of the heading angle derivative is shown with respect to the delayed actuation $u(t-\tau_\mathrm{s})$ for $\tau_\mathrm{s} = 0$ and $\tau_\mathrm{s} = 0.66$ seconds. Also illustrated is the steering gain estimate, $\hat{K}_\mathrm{s}$.

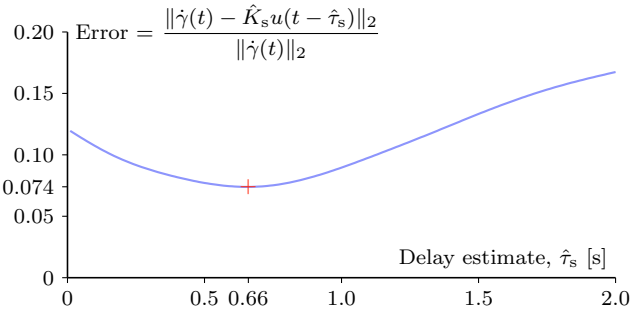

Fig. 8. Fit error as a function of the estimated delay, $\hat{\tau}_\mathrm{s}$, showing the delay estimate giving the minimum normalised mean square error. A value of $\hat{K}_\mathrm{s} = -10.05$ is used for the analysis shown.

$$\underset{\hat{K}_\mathrm{s},\hat{\tau}_\mathrm{s}}{\text{minimise}} \quad \left\|\dot{\gamma}(t) - \hat{K}_\mathrm{s}u(t-\hat{\tau}_\mathrm{s})\right\|_2.$$

Figure 8 shows the normalised RMS error of the model fit as a function of the steering input delay, $\hat{\tau}_\mathrm{s}$. The value of $\hat{K}_\mathrm{s}$ shown is $\hat{K}_\mathrm{s} = -10.05$ which is the corresponding $\hat{K}_\mathrm{s}$ minimiser for the normalised RMS model fit error. Also note that there is a reasonably broad range (more that $\pm 10\%$) of delay estimates, $\hat{\tau}_\mathrm{s}$, that give a good fit.

For the control adaptation, estimates $\hat{K}_\mathrm{s}$ and $\hat{\tau}_\mathrm{s}$ are calculated twice per figure-of-eight cycle during the traction phase using data from the 1 and 2 previous figure-of-eights. This typically gives between 500 and 3,000 data points for each estimate. This adaptation rate is relatively slow and best suited to changes in the dynamics due to varying tether length and changing wind conditions.

5. STATE ESTIMATION

The estimator design is driven by the available measurements. In the simplest case we have measurements of the tether angles and the tether length, taken at the ground station. These measurements are augmented by a wind sensor mounted on a 5 m. pole at the ground station. A suitably averaged wind direction estimate defines the wind window frame but the variability of the wind conditions leads to large errors if one uses the low altitude

measurement as an estimate of the velocity, v_w, that the kite experiences.

A particularly simple form of estimator comes from a discrete integration of the estimated position state, $\begin{bmatrix}\hat{\theta} & \hat{\phi} & \hat{r}\end{bmatrix}^T$. If the tethers are assumed to be straight then the tether angle and tether length measurements can be considered to be noisy measurement of the position state. If we further assume that the azimuth and elevation motions are decoupled we can create a simple integration model for the position state and its derivative. Assuming noise covariances on each of the measurements gives a simple steady-state Kalman filter. From the estimated derivative of the position state we can calculate and estimate, $\hat{\gamma}$, of the kite heading angle, γ. See Hesse et al. (2018) for a more complete derivation. This form of estimator is similar to that used in the experimental results presented in Section 6.

5.1 Sensor options

The assumption of straight tethers is not realistic, particularly during the retraction phase of the pumping cycle, and also during parts of the figure-of-eight traction phase. To address this problem we have investigated several other sensing options. These include:

Inertial measurement unit (IMU). We have flown kites with a Pixhawk Autopilot which is equipped with a Cortex M4 processor and several redundant sensors including a 3-axis accelerometer, 3-axis gyroscope, magnetometer, and barometer. Only the gyroscope measurements are used in our estimation systems.

Vision sensing. By mounting a wide-angle camera on the tether lead-out sheave the kite can be kept in the field of view of a vision sensing system. The camera is a GoPro HD Hero 2 video camera which can capture 1280×960 pixel video streams at 48 frames/second. This provides measurements of θ and ϕ that are not influenced by tether dynamics.

Radio localisation. Ultra-wide band time-of-flight radio sensors provide relative distance measurements over a range of several hundred metres and with an accuracy of less than 10 cm. This option has only been studied in simulation and so won't be described further in this paper.

Note that we have not included GPS systems in our configurations. The smaller rigid wing kites can fly figure-of-eight trajectories in as little as 6 seconds. The turning rates involved in these manoeuvres make it infeasible to maintain a lock on GPS satellites.

The image processing required to give kite altitude and azimuth estimates at the camera frame rate is relatively complex and beyond the scope of this paper. See Hesse et al. (2018) for more complete details.

5.2 Dual-unicycle estimator

The additional sensors considered now give either direct angular rate (via the IMU) or direct position (via vision sensing) measurements for the kite. Unlike the tether angle measurements, these kite measurements are not affected by the tether dynamics. The main difficulty in the estimator design is in dealing with the fact that some measurements are affected by additional unmodeled dynamics. To overcome this we create a second kite model which we assume to be measured by the tether angle and length sensors. This second model is coupled to the kite model, which is measured by the vision and/or IMU sensors. The effect of the tether dynamics is then captured by the coupling of these models. We refer to this model as a dual-unicycle model. The motivation for this type of model comes from Marshall (2005).

Name	Process model	Sensors
TA	Unicycle	tether angles
CG	Unicycle	camera/gyro
TCG	Dual unicycle	tethers/camera/gyro

Table 1. **Estimator configurations**

The elevation and azimuth of second unicycle model are denoted by θ^* and ϕ^* respectively,

$$\dot{\theta}^* = \frac{{v^*}_k}{r}\cos\gamma^* \tag{9}$$

$$\dot{\phi}^* = \frac{{v^*}_k}{r\cos\theta^*}\sin\gamma^*. \tag{10}$$

This model is a function of two coupling variables, ${v^*}_k$ and γ^* that are coupled to the kite velocity and heading via,

$${v^*}_k = v_k - v_{\text{offset}} \tag{11}$$

$$\gamma^* = \lambda\gamma(t - t_{\text{offset}}) \tag{12}$$

The offset variables v_{offset} and t_{offset} are estimated from data. This model is motivated by the experimental observation that the tether angles point to a location on the sphere that is moving more slowly and has a delay with respect to the kite. The parameter $\lambda \approx 1$ is needed to ensure that second unicycle also traces complete figures-of-eight.

In the dual-unicycle model structure the camera-based position measurements are treated as measurements of the kite position states θ and ϕ. The angular rate measurements from the gyroscope are used to calculate a measurement of the kite heading angle γ. However the tether angle measurements are considered as measurements of θ^* and ϕ^*.

In all cases sensor noise of specified covariance is included in the measurement models. The gyroscope measurements are also assumed to have noise driven drift. The estimator used was an unscented Kalman filter (UKF) (van der Merwe et al. (2004)). A more complete description of the Kalman filter design is given in Polzin et al. (2017).

5.3 Estimator configurations

Several estimator and sensor configurations have been studied in flight tests. Table 1 lists the sensors and estimator models used for the various configurations. The simplest estimation structure considered uses tether angles, gyroscope measurements of the angular rates and a simple unicycle model. The most complex adds the camera-based position measurement and a dual-unicycle model.

A summary of the estimators' performance is given in Table 2. The data is taken from 120 minutes of flight data. The errors are calculated with respect to the kite position determined on a post-processed image. The TA

Name	$\hat{\gamma}$ error [deg.]	$(\hat{\theta}, \hat{\phi})$ error [deg.]
TA	21	4.1
CG	11	0.7
TCG	9.7	0.7

Table 2. **Estimator performance**

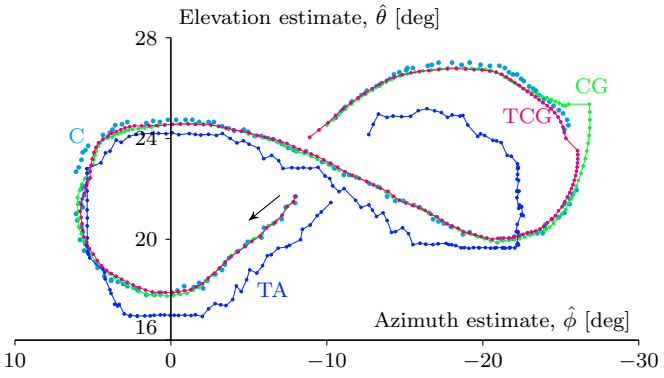

Fig. 9. Estimator comparison in the azimuth/altitude frame from the point of view of the ground station. The three estimators are TA (blue), CG (green), and TCG (magenta). For comparison the camera image measurements are also shown (C, cyan). Camera measurements were lost at the right-hand side of the figure-of-eight trajectory.

estimator has the worst performance because the tether angle measurements are assumed to be unbiased and this is clearly not the case. The addition of a camera-based sensor (in CG and TCG) significantly improves the performance of these estimators. When tether angles are included in the TCG estimator the use of the dual-unicycle process model implicitly allows for a bias in the tether angle measurements.

The estimators' performance is also compared on a partial figure-of-eight trajectory in Figure 9. For comparison the projections onto the wind window (from the point of view of the ground-station) of the camera-based position measurements are also shown. The bias in the tether angle-based estimator (TA) is very large over most of the trajectory.

The same flight data is used in the $\hat{\gamma}$ estimates shown in Figure 10. In the time domain the delay in the $\hat{\gamma}$ estimate from the tether angle-based estimator configuration (TA) is clear.

The flight data in Figures 9 and 10 also contains a period where the camera loses track of the kite (grey-shaded area). Both the CG and TCG estimators accumulate bias due to the loss of the most effective sensor. The TCG model performs better in this circumstance as it is able to use information from the tether angles to maintain a better estimate.

Figure 11 illustrates the difference between tether angle measurements and the CG estimator on a frame from the camera sensor. The CG estimates are compared in the image plane to the projected tether angles. The kite is also visible confirming the accuracy of the CG estimator.

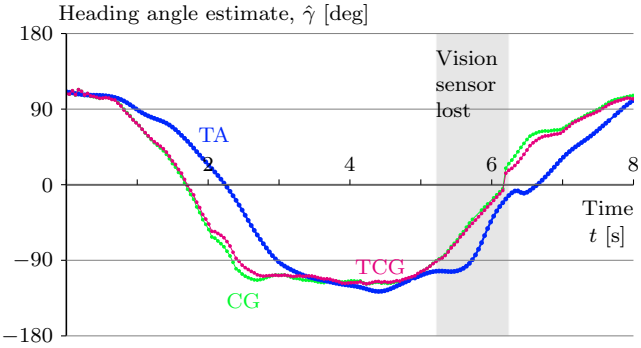

Fig. 10. Heading angle estimation performance. The three estimates show the performance of each estimator of γ as a function of time. The data corresponds to the figure-of-eight trajectory shown in Figure 9. The grey region indicates the part of the trajectory where the camera-based position measurement was lost.

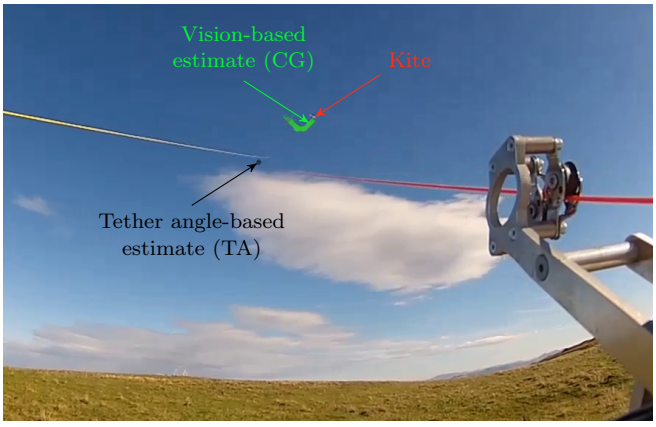

Fig. 11. Comparison of the tether angle and camera-based position measurements. Overlaid on the image are the projected kite position, as estimated from tether angles (TA), and the last 20 estimates from the vision-based estimator (CG).

6. EXPERIMENTAL ADAPTIVE CONTROL

To illustrate the online identification and controller adaptation we present results from a tow test experiment performed on an airfield in Switzerland in December 2016. Further details on these experiments can be found in Wood et al. (2017b). The kite and winch system is towed behind a vehicle and with no ambient wind this allows us to create measurable wind conditions with respect to the kite. Figure 12 shows the experimental configuration.

The runway length limits the experiments to approximately 180 seconds of flight and a representative trajectory is illustrated in Figure 13. The ground station has a controller adjusting the tether lengths in response to a tether force measurement. This gives some change in tether length, $r(t)$, over the duration of an experiment and so $r(t)$ is also recorded.

The steering delay, τ_s, was up to 0.7 sec. and the controllable part of the MPC horizon was 0.3 sec. giving a total horizon of 1.0 sec.. This is a relatively small proportion of a single figure-of-eight trajectory (typically between 6 and 20 seconds in these experiments).

Fig. 12. The ground station, shown on the left, contains the winches, tether feed-out system, and the monitoring/control hardware. The towed configuration is shown on the right. A pole-mounted anemometer and wind vane provide wind speed and direction measurements.

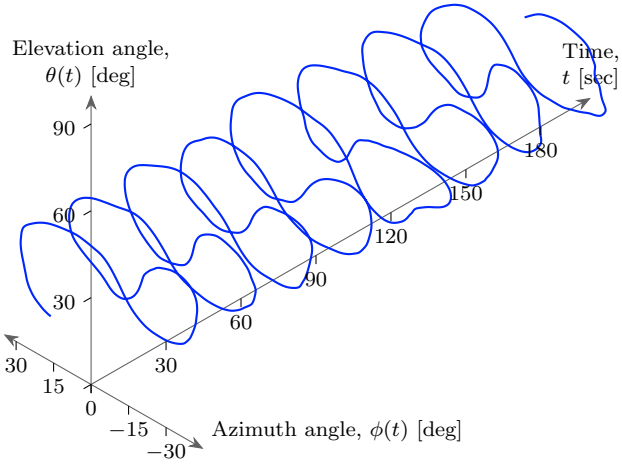

Fig. 13. Tow test experiment showing the elevation angle, $\theta(t)$, and azimuth angle, $\phi(t)$, as a function of time.

The estimates $\hat{K}_s$ and $\hat{\tau}_s$ are calculated with each of the two crossings of the centre of the wind window per figure-of-eight trajectory. For the controller bandwidth and γ_{ref} trajectory band-limit calculation in (7) and (8) we assume a 20% uncertainty on $\hat{K}_s$ and $\hat{\tau}_s$.

Figure 14 shows the measured wind velocity, v_w, and tether length, $r(t)$, during the tow test experiment. The wind speed varies over a factor of two while the tether length varies between 80 and 100 metres. The resulting estimates of the delay, $\hat{\tau}_s$, and steering gain, $\hat{K}_s$, are also shown. The delay ranges between 0.6 and 0.85 seconds. During the 85 to 95 second interval there is a large increase in the tether length, $r(t)$, and the constant tether length model fit gives a bad estimate. This is detected in the analysis and flagged as an unreliable estimate. The estimate of the steering gain ranges from -4.5 to -6 and shows significant half-cycle to half-cycle variation.

The effect of the γ_{ref} tracking band limitation is shown in Figure 15. The $|\dot{\gamma}_{ref}|$ limit in (8) is shown together with the actual value of $|\dot{\gamma}_{ref}|$. The γ_{ref} reference trajectory derivative hits its limit at a significant number of time instances indicating that the adaptation gains are imposing meaningful limits on the steering trajectory.

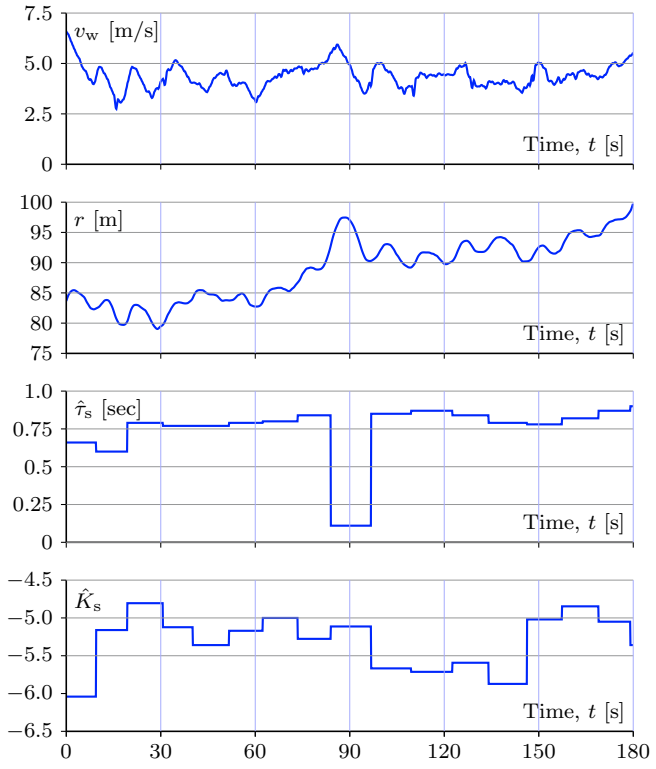

Fig. 14. Measurements of the wind speed, v_w, and the tether length, $r(t)$; estimates of the actuation delay, τ_s, and steering gain, K_s.

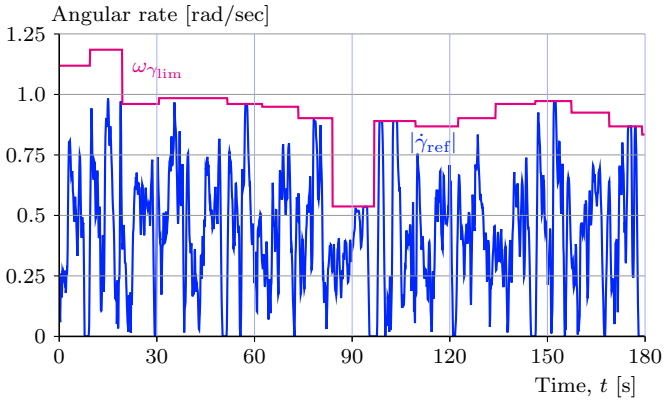

Fig. 15. Bound on the rate of change of the commanded heading angle, $\omega_{\gamma_{lim}}$, and resulting magnitude of the rate of the commanded orientation, $|\dot{\gamma}_{ref}|$.

7. DISCUSSION

Effectively flying power generating kites raises a variety of interesting questions for modeling, identification and control. There is a significant amount of uncertainty in the dynamics that arises primarily from the uncertain aerodynamic forces on the kite and this is particularly challenging in the lower cost soft-kite configurations. The problem is further compounded by significant variations in the wind characteristics. We have pursued a strategy of developing relatively simple models and identifying key parameters during flight operation. These are then used to adjust the controller gains, and to set constraints

on the optimisation problems that calculate the desired trajectories. Simple estimators, based on tether angles and tether length, can be used for the control. However the estimation performance is significantly improved by sensors, such as camera sensors, that are not affected by the dynamics of the tethers. Flight tests illustrate that the adaptive approach is feasible and there is clearly much more that can be done towards achieving the goal of robust flight performance in a wide range of wind conditions.

ACKNOWLEDGMENTS

We would like to thank Corey Houle, Damian Aregger, and Jannis Heilmann from the Fachhochschule Nordwestschweiz (FHNW) and Rolf Luchsinger, Flavio Gohl, Cédric Galliot, Florian Bezard and Dino Costa from TwingTec for providing the experimental facilities and support.

REFERENCES

Breuer, J.C.M. and Luchsinger, R.H. (2010). Inflatable kites using the concept of tensairity. *Aerospace Science and Technology*, 14(8), 557–563.

Canale, M., Fagiano, L., and Milanese, M. (2007). Power kites for wind energy generation. *IEEE Control Systems Magazine*, 27(6), 25–38.

Costello, S., Francois, G., and Bonvin, D. (2015). Directional real-time optimization applied to a kite-control simulation benchmark. In *Proc. European Control Conference*, 1594–1601. Linz, Austria. doi: 10.1109/ECC.2015.7330765.

Diehl, M. (2001). *Real Time Optimization for Large Scale Nonlinear Processes*. Ph.D. thesis, Univ. of Heidelberg, Germany.

Erhard, M. and Strauch, H. (2013). Control of towing kites for seagoing vessels. *IEEE Trans. Control Systems Technology*, 21(5), 1629–1640.

Fagiano, L. (2009). *Control of tethered airfoils for high-altitude wind energy generation*. Ph.D. thesis, Politecnico di Torino, Italy.

Fagiano, L., Zgraggen, A.U., Morari, M., and Khammash, M. (2014). Automatic crosswind flight of tethered wings for airborne wind energy: Modeling, control design, and experimental results. *IEEE Trans. Control Systems Technology*, 22(4), 1433–1447.

Hesse, H., Polzin, M., Wood, T.A., and Smith, R.S. (2018). Visual motion tracking and sensor fusion for ground-based kite power systems. In R. Schmehl (ed.), *Airborne Wind Energy*. Springer.

Houska, B. and Diehl, M. (2006). Optimal control of towing kites. In *IEEE Conf. on Decision & Control*, 2693–2697. San Diego, CA, USA.

Jehle, C. and Schmehl, R. (2014). Applied tracking control for kite power systems. *J. Guidance, Control, & Dynamics*.

Lansdorp, B. and Ockels, W. (2005). Design of a 100 MW laddermill for wind energy generation from 5 km altitude. In *World Congress on Recovery Recycling and Reintegration*. Beijing, China.

Loyd, M. (1980). Crosswind kite power. *Journal of Energy*, 4(3), 106–111.

Luchsinger, R., Aregger, D., Bezard, F., Costa, D., Galliot, C., Gohl, F., Heilmann, J., Hesse, H., Houle, C., Wood, T.A., and Smith, R.S. (2018). Pumping cycle kite power with Twings. In R. Schmehl (ed.), *Airborne Wind Energy*, chapter 24. Springer.

Makani (2018). Online: `x.company/makani/`.

Marshall, J. (2005). *Coordinated Autonomy: Pursuit formations of Multivehicle Systems*. Ph.D. thesis, Univ. of Toronto.

Ockels, W. (2001). Laddermill, a novel concept to exploit the energy in the airspace. *Aircraft Design*, 4(2-3), 81–97.

Patterson, M.A. and Rao, A.V. (2014). GPOPS-II: A MATLAB software for solving multiple-phase optimal control problems using hp-adaptive gaussian quadrature collocation methods and sparse nonlinear programming. *ACM Trans. Math. Softw.*, 41(1), 1–37. doi: 10.1145/2558904.

Polzin, M., Wood, T.A., Hesse, H., and Smith, R.S. (2017). State estimation for kite power systems with delayed sensor measurements. In *Proc. IFAC Control World Congress*. Toulouse, France.

Schmehl, R. (ed.) (2018). *Airborne Wind Energy*. Springer.

Schmehl, R., Noom, M., and van der Vlugt, R. (2013). Traction power generation with tethered wings. In U. Ahrens, M. Diehl, and R. Schmehl (eds.), *Airborne Wind Energy*, chapter 2, 23–45. Springer.

TwingTec (2018). Online: `twingtec.ch`.

van der Merwe, R., Wan, E., and Julier, S. (2004). Sigma-point Kalman filters for nonlinear estimation and sensor-fusion: Applications to integrated navigation. In *Guidance, Navigation, & Control Conf.*, 16–19. Providence, RI, USA.

Wood, T.A., Ahbe, E., Hesse, H., and Smith, R.S. (2017a). Predictive guidance control for autonomous kites with input delay. In *Proc. IFAC Control World Congress*, volume 50, 13276–13281. Toulouse, France.

Wood, T.A., Hesse, H., and Smith, R.S. (2017b). Predictive control of autonomous kites in tow test experiments. *IEEE Control Systems Letters*, 1(1), 110–115.

Wood, T.A., Hesse, H., Zgraggen, A., and Smith, R.S. (2015a). Model-based flight path planning and tracking for tethered wings. In *Proc. Control & Decision Conf.*, 6712–6717. Osaka, Japan.

Wood, T.A., Hesse, H., Zgraggen, A.U., and Smith, R.S. (2015b). Model-based identification and control of the velocity vector orientation for autonomous kites. In *Proc. American Control Conf.*, 2377–2382,. Chicago, IL, USA.

Zgraggen, A.U. (2015). *Automatic Power Cycles for Airborne Wind Energy Generators*. Ph.D. thesis, Swiss Federal Inst. Tech. (ETH).

Zgraggen, A.U., Fagiano, L., and Morari, M. (2015). Real-time optimization and adaptation of the crosswind flight of tethered wings for airborne wind energy. *IEEE Trans. Control Syst. Techn.*, 23(2), 434–448.